Supporting Information

Surface modified halloysite nanotubes with different lumen diameters as drug carriers for cancer therapy

Juan Liao[a], Dongyue Wang[a], Aidong Tang[b], Liangjie Fu[a,c,d], Jing Ouyang[ad], Huaming Yang[a,c,d*]

[a] *Hunan Key Lab of Mineral Materials and Application, School of Minerals Processing and Bioengineering, Central South University, Changsha 410083, China*

[b] *School of Chemistry and Chemical Engineering, Central South University, Changsha 410083, China*

[c] *Engineering Research Center of Nano-Geomaterials of Ministry of Education, China University of Geosciences, Wuhan 430074, China*

[d] *Faculty of Materials Science and Chemistry, China University of Geosciences, Wuhan 430074, China*

[*] Correspondence: hmyang@csu.edu.cn (H. Yang)

Table of contents

Experimental section

Materials

Halloysite nanotubes (HNTs) powders were purchased from Huzhou, Zhejiang Province (China). PTX and DSPE-PEG_{2000}-NH_2 (≥ 95%) were purchased from Sigma-Aldrich (St. Louis, MO). Fluorescein isothiocyanate (FITC), dimethyl sulfoxide (DMSO), methanol, and acetonitrile were provided by Aladdin (Shanghai, China). Hoechst was purchased from Beyotime Institute of Biotechnology (Shanghai, China). All reagents were used as received without further purification. HT-29 human colon cancer cells were purchased from Tsingke (Beijing, China), MDA-MB-231 cancer cells were purchased from iCell Bioscience Inc (Shanghai, China).

Expanding the lumen diameter of the halloysite

HNTs were pretreated via the combination of high-speed shear homogenization and two-step uniform viscosity centrifugation as reported in our previous work [1]. Then, 1 g of pretreated HNTs were treated with 100 mL, 2 mol/L of sulfuric acid (H_2SO_4) solution at 90 °C under constant stirring for different amounts of time (ranging from 0.5 h to 7 h). The suspension was then filtered, washed with distilled water, and dried at 80 °C overnight.

Surface free energy calculation

The interactions between drug molecules and HNT samples are determined by their surface properties. Therefore, accurately determining the surface energy between the drug molecules and HNT samples leads to a basic understanding of the drug loading mechanism among HNTs with different inner diameters. The contact angles experiments were carried out five times and the average values were presented. The total surface free energy γ is composed of two parts: the nonpolar part γ^{LW} (i.e., Lifshitz-van der Waals) and the polar part γ^{AB} (i.e., Lewis acid-base) according to the van Oss-Chaudhury-Good theory [2-4]. The non-polar dispersive component is mainly attributed to London forces, while the polar component (Lewis acid-base interactions) is mainly associated with hydrogen bonding and the behavior of the electron donor-acceptor (i.e., γ^- and γ^+). The surface free energy of the solid γ_S and the liquid γ_L can be calculated as :

$$\gamma_s = \gamma_s^{LW} + \gamma_s^{AB} = \gamma_s^{LW} + 2\sqrt{\gamma_s^+ \gamma_s^-} \quad (1)$$

$$\gamma_L = \gamma_L^{LW} + \gamma_L^{AB} = \gamma_L^{LW} + 2\sqrt{\gamma_L^+ \gamma_L^-} \quad (2)$$

According to the Dupre equation, the solid-liquid interfacial free energy γSL is expressed as:

$$\gamma_{SL} = \gamma_S + \gamma_L - 2(\sqrt{\gamma_S^{LW} \gamma_L^{LW}} + \sqrt{\gamma_S^+ \gamma_L^-} + \sqrt{\gamma_S^- \gamma_L^+}) \quad (3)$$

By combining Eqs. (1), (2), and (3), and Young's equation, Eq. (4) is obtained

$$(\gamma_L^{LW} + 2\sqrt{\gamma_L^+ \gamma_L^-})(1 + \cos\theta) = 2(\sqrt{\gamma_S^{LW} \gamma_L^{LW}} + \sqrt{\gamma_S^+ \gamma_L^-} + \sqrt{\gamma_S^- \gamma_L^+}) \quad (4)$$

Based on Eq. (4), the solid surface energy and its components can be obtained by measuring the contact angles of three different liquids (two polar liquids are required).

Loading of PTX

PTX was employed as a model drug molecule for the loading experiments. DSPE-HNTs-PTX were

prepared by a facile surfaces modification as described elsewhere [5]. 2 mg of HNT were dispersed in 200 μL DMSO and 1.2 mg DSPE-PEG_{2000}-NH_2 were dissolved in 120 μL DMSO, followed by these two solutions mixed. Next, 0.4 mg of PTX dissolved in 40 μL DMSO were added to acquire a total volume of 0.36 mL of a mixed solution as the oil phase. Thereafter, the oil phase mixture was added dropwise to 40 mL of deionized water solution under stirring at 1200 rpm for 1 min; simultaneously, DSPE-HNTs-PTX was obtained. Additionally, DSPE-HNTs-PTX were washed three times with deionized water to remove the free PTX.

***In vitro* release study**

The *in vitro* drug release test was conducted. Thus, halloysite was placed in the release medium (PBS, pH 6.8 and pH 7.4) containing 0.5% SDS to obtain the concentration of 0.25 mg/mL at 37 °C, followed by shaking at 180 rpm. At specified time points (0.5, 1, 2, 4, 6, 8, 10, 12, 24, 48, and 72 h), 1 mL of the dissolution media was collected and supplemented with the same amount of fresh dialysis fluid. The amount of PTX released was measured using HPLC (SPD-10AV, Waters 515).

Determination of PTX loading and releasing

To determine the loading capacity of the HNT sample, 20 mg of DSPE-HNTs-PTX, accurately weighed, were dissolved in 2 mL methanol. The suspension was then dispersed with ultrasonic dispersion at 37 °C for 4 h. The supernatant collected was diluted with water and acetonitrile (water: methanol: acetonitrile=40:30:30) and the amount of PTX released was measured using HPLC. For the determination of PTX loading and releasing, chromatographic separation was performed on an Agilent XDB-C18 column (150 mm×4.6 mm, 5 μm) using water-methanol-acetonitrile (40:30:30, v/v/v) as mobile phase at a detection wavelength of 227 nm. The encapsulation efficiency (EE) and drug loading (DL) capacity of PTX was calculated as below.

$$\text{EE (\%)} = \text{Weight of PTX encapsulated/Weight of PTX added} \quad (5)$$

$$\text{DL (\%)} = \text{Weight of PTX encapsulated/Weight of NPs} \quad (6)$$

Release Kinetic Models

To well-study the release behaviors of DSPE-HNTs-PTX, the release experimental data were modeled by theoretical models including Peppas model and Higuchi model [6,7], and adjusted linear regression (R^2) was chosen as the evaluation index. First, a Peppas model semiempirical equation was given as below.

$$M_t / M_\infty = at^b \quad (7)$$

where “a” is the kinetic constant and “b” is an exponent identifying the diffusion mechanism. M_t and M_∞ are cumulative release amounts at time t and at infinite time, respectively. When b = 0.5, Peppas model translates into Higuchi model as below:

$$M_t / M_\infty = at^{1/2} \quad (8)$$

Cells culture

HT-29 human colon cancer cells were cultured in Dulbecco's modified Eagle's medium (DMEM) supplemented with 10% fetal bovine serum and 1% penicillin/streptomycin in an atmosphere containing 5 % CO_2.

MTT assay

The cytotoxic activity of DSPE-HNTs-PTX to HT-29 cells for 24 h was assessed by the MTT assay. Briefly, HT-29 cells were seeded in 96-well plates at a density of 2.0×10^4 cells/well and incubated with DMEM at 37 °C in an atmosphere containing 5% CO_2 for 24 h. Subsequently, HT-29 cells were incubated with free PTX, free PTX plus halloysite, DSPE-HNTs-PTX with different inner diameters at different PTX concentrations (0.25-10 μg/mL), respectively. Then, free materials were removed and replaced with 100 μL DMEM. The optical density value at 490 nm was measured using a microplate reader (EnVision Xcite/HTS; PerkinElmer, USA). The cell viability with data from three parallel wells was calculated.

Cellular uptake assay

Cellular uptake and internalization efficiency of FITC-HNT sample in HT-29 cells were qualitatively using fluorescence microscopy and quantitatively with flow cytometry. For qualitative analysis, HT-29 cells were first incubated in a CLSM-special culture dish until the cell density reached 50~60 %, and a fresh medium containing the nanocomposites (2 mL, 50 μg/mL) was added. Cells were then incubated for 24 h. After incubation, cells were then washed three times and stained using Hoechst. The cells were stored in the dark until being visualized by CLSM (LSM880; Zeiss, Germany), and the wavelength of the stimulating laser of FITC was 495 nm. For quantitative analysis, HT-29 cells were cultured in 96-well plates at a density of 2×10^5 cells per well and cultured for 24 h. The old cell culture medium was replaced by the FITC-HNT sample and the cells were incubated at 37 °C and 5% CO_2 for 4 h. After incubation, the cells were then entirely washed with PBS and collected. The cellular uptake efficiency of HT-29 cells was determined by flow cytometry (BD Accuri C6 Plus; BD, USA).

***In vivo* Anti-tumor study**

BALB/c mice (5~6 weeks old, male) were bought from Vital River Laboratory Animal Technology Co., Ltd (Beijing, China). All animal experiments were performed in accordance with the National Institute of Health Guidelines under the protocols, approved by the Ethics Committee of Hunan Drug Safety Evaluation and Research Center. To establish the tumor model *in vivo*, MDA-MB-231 cells (2×10^6 cells/mL) were subcutaneously injected into BALB/c mice for 14 days. When the tumors reached about 100-200 mm^3, MDA-MB-231-Bearing mice were randomly divided into five groups (5 animals per group) and treated with (1) Free PTX, (2) Saline, (3) DSPE-$HNTs_{46}$-PTX, (4) DSPE-$HNTs_{29}$-PTX, (5) DSPE-$HNTs_{15}$-PTX. The doses of Free PTX and DSPE-HNTs-PTX were 4 mg/kg and 22.7 mg/kg, respectively. The tumor volume and body weight were measured every 2 days for 14 days since the first treatment. The tumor volumes were calculated as $W^2\times L/2$, where W and L were the lengths in minor and major of the tumor, respectively. The relative body weight was defined as W/W_0 (W_0 is the bodyweight of mice on the first day before any treatment). To further evaluate the antitumor activity, a histology study was also carried out. The tumor tissues from each group were dissected, stained with hematoxylin and eosin (H&E), TdT-mediated dUTP Nick-End Labeling (TUNEL), and observed by optical microscopy. The apoptotic cells were quantified in five randomly selected fields and shown by the percentages of the total number of cells.

Statistical analysis

Statistical analysis was carried out using SPSS 9.0 software, and all data were presented as means ±

standard deviation (SD). The statistical significance was obtained by one-way ANOVA with Tukey's post hoc test. The differences were considered to be statistically significant for a p-value <0.05 (*P < 0.05, **P < 0.01, ***P < 0.001).

Characterization

The Al content leached was determined by Inductively Coupled Plasmas Atomic Emissive Spectrometry (SPECTROBLUE, SPECTRO, Germany). The morphology and structure were characterized using two TEMs (FEI Tecnai G2 F20, 200 kV, and JEOL JEM-2010). The phase purities of $HNTs_{15}$, $HNTs_{23}$, $HNTs_{29}$, $HNTs_{32}$, and $HNTs_{46}$ were analyzed by XRD (D8 Advance; Bruker, Germany) with Cu Kα-radiation (using CuKa radiation, k=1.5418 Å, 40 kV, 200 mA) in the 2θ range of 5°~80°. Scanning electron microscopy (SEM) images were obtained using a Mira3 LMU (Tescan, Czech Republic). FTIR spectra were recorded using a Shimadzu FTIR 8120 spectrometer from 4000 to 400 cm^{-1}. Particle size distribution and Zeta potential values were measured on a Zetasizer Nano ZS particle analyzer (Malvern Zetasizer NANO ZS90; Malvern, UK). The contact angle of HNTs with different inner diameters was determined using the sessile drop technique on a water contact angle analyzer (DSA 100, 142 Kruss, Germany) utilizing RO water, methanamide, and 1-Bromonaphthalene as the probe liquid. The isothermal N_2 gas adsorption-desorption was obtained using ASAP 2020 Plus HD88 (BET; Micromeritics, America). Solid-state magic-angle spinning nuclear magnetic resonance (MAS NMR) spectra were recorded using a Bruker AMX400 spectrometer to characterize the local structure around the Si atoms in the HNT sample, with frequencies of 79.49 MHz for ^{29}Si.

Supplementary Results

TEM analysis

$HNTs_{15}$ exhibits a typical tubular structure of cylindrical shape with an open-ended lumen (Fig. S2a). The length of the tube is about 100~500 nm, and the diameter of the tube lumen is about 10~25 nm. Due to the rich hydroxyl on the surface, HNT is easy to disperse in an aqueous solution and exhibits uniform size and good dispersion under a transmission electron microscope. Compared with the $HNTs_{15}$, the inner-diameter of $HNTs_{23}$ is enlarged (the inner diameter increased 52%) and becomes rough. The external diameters of the tubes remained smooth, indicating that etching takes place solely in the inner lumen. When the dealumination reached 60%, which refers to expanding the lumen diameter to 29 nm, the tubes preserved their geometry, while some holes appeared on halloysite walls at the higher level of etching. Upon further acid leaching, $HNTs_{32}$ and $HNTs_{46}$ exhibited a significantly increased lumen diameter while the wall became increasingly thinner. The tubular morphology was still maintained while silica nanoparticles of 10-20 nm diameter from dealuminated halloysite walls were observed. Compared to $HNTs_{15}$ (Fig. S10a), the lattice spacing of $HNTs_{29}$ increases to 0.7 nm, corresponding to the (001) plane of the halloysite. The 46 nm diameter HNT sample shows a lattice spacing of 0.3 nm that corresponds to the (011) plane of SiO_2. These findings indicate that the edge surface (100) of the halloysite decreases during the process of acid leaching. In addition, SiO_2 NPs adhered to the surface of $HNTs_{46}$ have been detected, which is consistent with the XRD results (Fig. S3a) that $HNTs_{46}$ loss the part of the tube wall crystallinity and exists in the form of the

basic silicon-oxygen tetrahedron.

XRD analysis

Fig. S3a (ESI†) shows the XRD patterns of the halloysite samples with different inner diameters, in which $HNTs_{15}$ reflects the basic phase of halloysite with water purification. The diffractions peaks at 12.11, 20.01, 24.86, 35.16, 54.62 and 62.67° correspond to the base reflections on (001), (100), (002), (110), (210) and (300) planes, respectively. $HNTs_{15}$ shows characteristic peaks at 12.37 and 24.96°, corresponding to 7.35 Å and 3.58 Å spacings, respectively. The d001 peak at 7.3 Å corresponds to the multilayer wall packing. It is noted that the diffraction peaks which appeared at approximately 18.09 and 30.04° are related to the impurity phases of alunite (JCPDS PDF No. 73-1652). While very small amounts of iron oxide may have existed since the peak around 18 and 30 ° can be overlapped by the coexistence of alunite and iron oxide (JCPDS PDF No. 89-0950). As is can be seen from Fig. S3a, the reflection of the halloysite was not shift and all the peaks were seen with low intensity during the process of acid leaching. and it was noted that a wide peak of amorphous SiO_2 was observed in $HNTs_{46}$. This observation revealed that the structural regularity and the diffraction peak intensity decrease during the dealumination. For further expanding the lumen diameter, the residual structure of the halloysite composed of invisible SiO_2 was detached while some had adhered to the surface of the halloysite. Hence, $HNTs_{46}$ loses the part of the tube wall crystallinity and exists in the form of the basic silicon-oxygen tetrahedron. It is noted that the peak intensity of iron oxide decreases when the inner diameter of the tube increases. This is because iron oxide in halloysite reacts more fully with sulfuric acid with the increase of acid leaching degree, indicating that iron oxide impurities were reduced and the purity of halloysite was improved while acid leaching was used for inner-diameter expanding.

MAS NMR spectra analysis

MAS NMR spectra of ^{29}Si elements in the halloysite samples with different inner diameters are included in Fig. S3b (ESI†). It revealed three types of silicon atoms existing in partially dealuminated samples. The sharp 89.4 ppm signal is assigned to Q^3-type $Si(OSi)_3(OAl_2)$ sites, where each silicon has two seconds nearest neighbor octahedral aluminum from the nearby aluminum hydroxide layer of unreacted halloysite. The broader 98 ppm (97 to 99 ppm) peak is assigned to newly formed Q^3-type silicon sites with one-second nearest-neighbor aluminum (Si $(OSi)_3$-(O^+AlH)). The signal at 108 ppm (107 to 109 ppm) is assigned to newly formed Q^4-type $Si(OSi)_4$ sites of amorphous silica-like regions in these dealuminated solids.

Particle size and distribution analysis

Dynamic light scattering (DLS) was used to determine the hydrodynamic diameter and size distribution of the HNT sample (Fig. S8). Originally, $HNTs_{15}$ shows a broad distribution range. It is noted that the overall size distribution of $HNTs_{23}$ was shifted to the left, which indicates that halloysite nanotubes were non-agglomerated under the combination of magnetic stirring and acid leaching. D_{50} measured by DLS are 351.6±8.8, 257.9±2.8, 321.3±3.8, 294.4±1.4, and 345.0±20.7 nm. Average sizes of $HNTs_{29}$ $HNTs_{32}$ and $HNTs_{46}$ increase slightly, while still less than that of $HNTs_{15}$. This may be due to the etching level (50~60% dealumination), with the inner diameter expanding, leftover SiO_2 partially aggregates and forms tiny nanoparticles which are adsorbed on the outside or port of halloysite was monitored with dynamic light

scattering. This is consistent with SEM and TEM observations.

Specific surface area and pore structure distribution analysis

The nitrogen adsorption/desorption isotherms of the HNT sample can be classified as a combination of curves II and IV(a). This combination describes very well the porosity (macro- and mesopores) contained in the HNT sample (Fig. S9a). Hysteresis loops are type H3 in all cases and the area of the hysteresis loop increases with the increase of tube diameter. Fig. S9b shows a multimodal distribution of pore size. The specific surface areas of the HNT sample obtained by the BJH (Barrett-Joyner-Halenda) calculation method were 54.04, 79.20, 98.63, 113.48, and 115.80 m^2/g, respectively (Table S4). Micropores exist in halloysite nanotubes, while most of them are mesoporous. For $HNTs_{15}$, the maximum populations of pores are centered with radii of about 3.6, 12.4, and 32.6 nm. After the inner diameter expanding by acid treatment, populations of pores increased in the central site at 3.6 nm were shifted to the right, nonetheless, pores in the central site at 12.4 and 32.6 nm were both shifted to the left. The proportion at 12.4 nm increased while that of 32.6 nm decreased, which indicating that the mesoporous of this part increased. This result is partly due to the slit pore formed after the dehydration of the halloysite. On the other hand, it is speculated that the etched dinner wall with some SiO_2 particles absorbed and agglomerated, may result in the decrease of diameter in micropore. In addition, the average pore sizes of the HNT sample mentioned above were 20.8, 17.3, 14.4, 13.1, and 15.1 nm, respectively. While the pore volume did not change significantly.

Release characteristic of PTX from HNT samples

In comparison, Fig. S11 (ESI†) shows that the release of free PTX is approximately 89 % within 8 h. The faster release of free PTX does not beneficially assist the extension of its circulation time and leads to various adverse side effects. According to Fig. S12a (ESI†), there is a burst release of PTX within the HNT sample during the first 30 min. The burst release of PTX may be due to weak interactions between the HNT and PTX, allowing some drugs to escape from the surfaces and lumen into the solution. A partial burst release is inevitable. Increasing lumen diameter and associated HNT surface area should offer better control and limit the “initial burst” bolus. As the degree of acid leaching increases, some of the micropores increased and the mesoporous center size is reduced which are attributed to the delay of drug release, especially in an acidic environment (Table S4, ESI†). In addition to introducing the possibility of a stimuli-responsive behavior, we expect that the undesired leaching of drugs during circulation in the human body can be reduced. The PTX release profile is shown in Fig. S12b (ESI†). Fig. S13 (ESI†) illustrates the fitted curves of PTX released from HNT samples, and the fitted results are shown in Table S5 (ESI†).

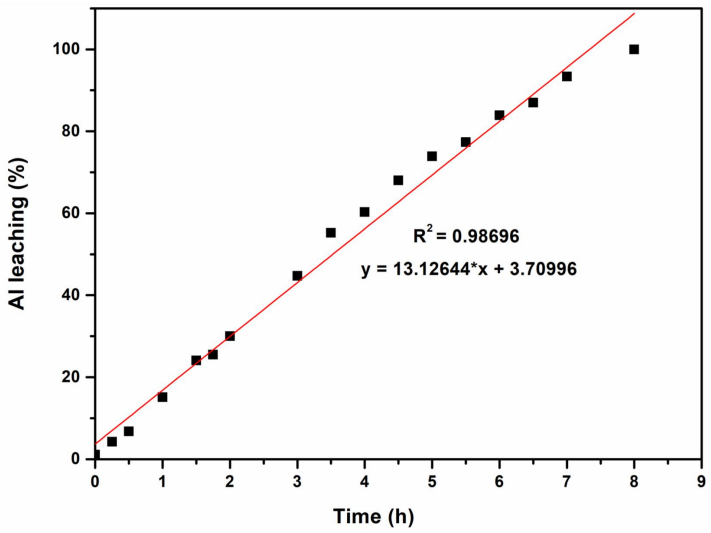

Figure S1. The alumina leaching rate of HNTs varies with time by treatment with H_2SO_4.

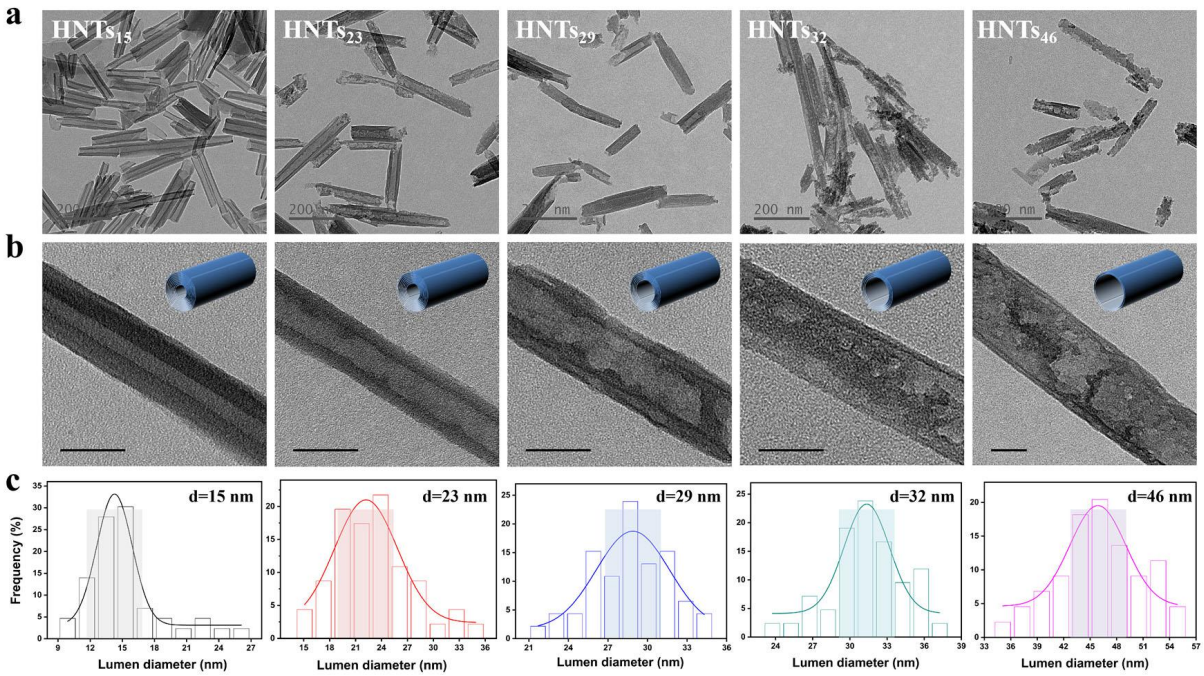

Figure S2. (a) and (b) TEM images of halloysite. (c) Histogram of lumen diameters of etched. Scale bar = 50 nm.

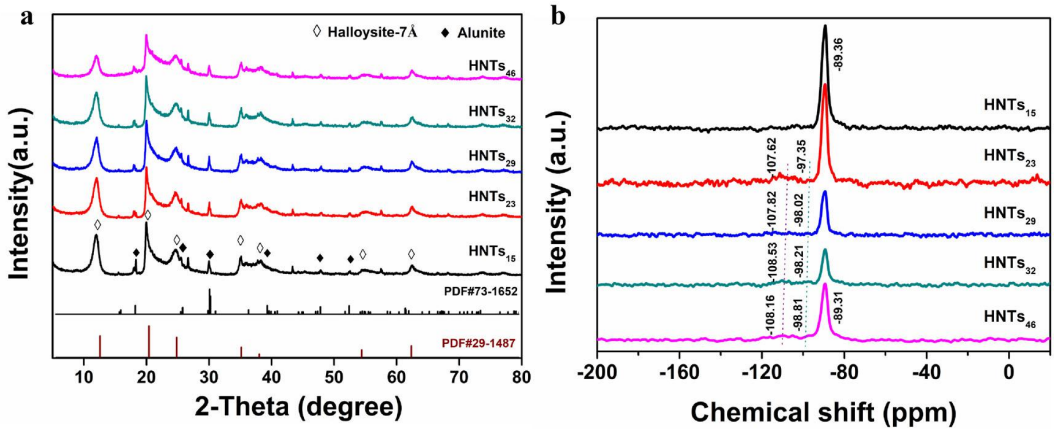

Fig. S3. (a) XRD patterns. (b) ^{29}Si MAS NMR spectra of HNTs samples with different inner diameters.

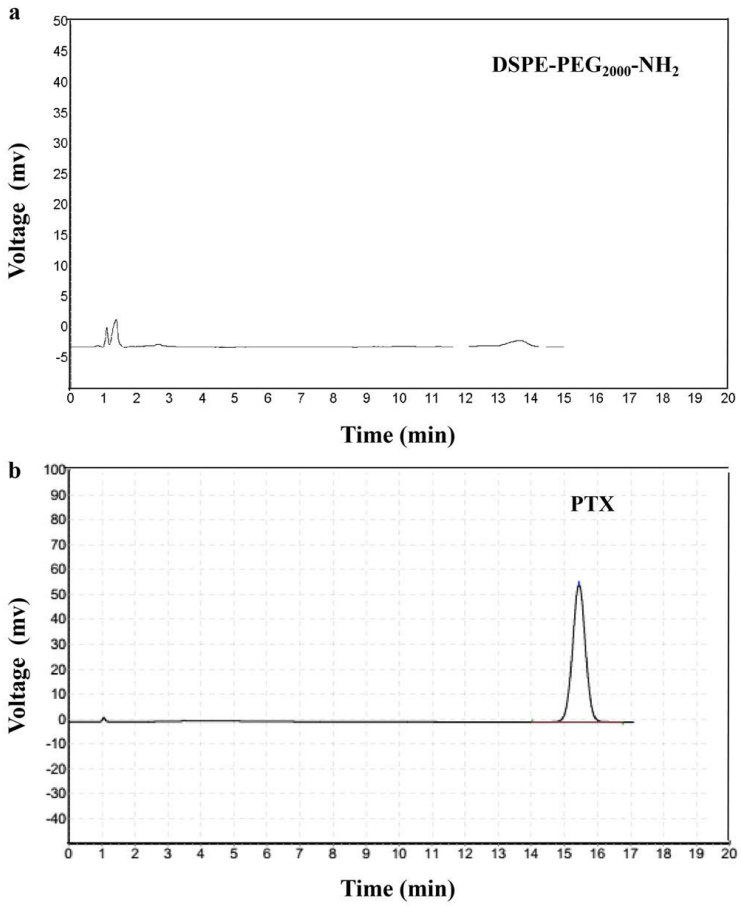

Fig. S4. High-performance liquid chromatography of (a) DSPE-PEG_{2000}-NH_2 and (b) PTX.

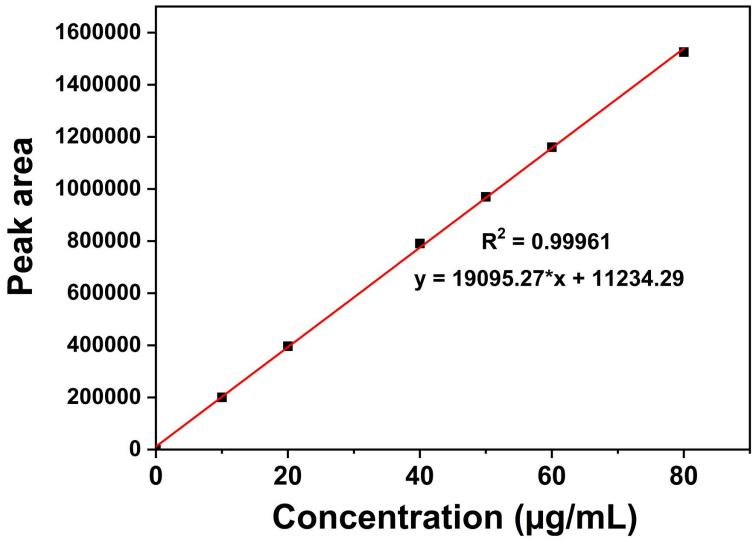

Fig. S5. Standard curve of PTX in the mobile phase.

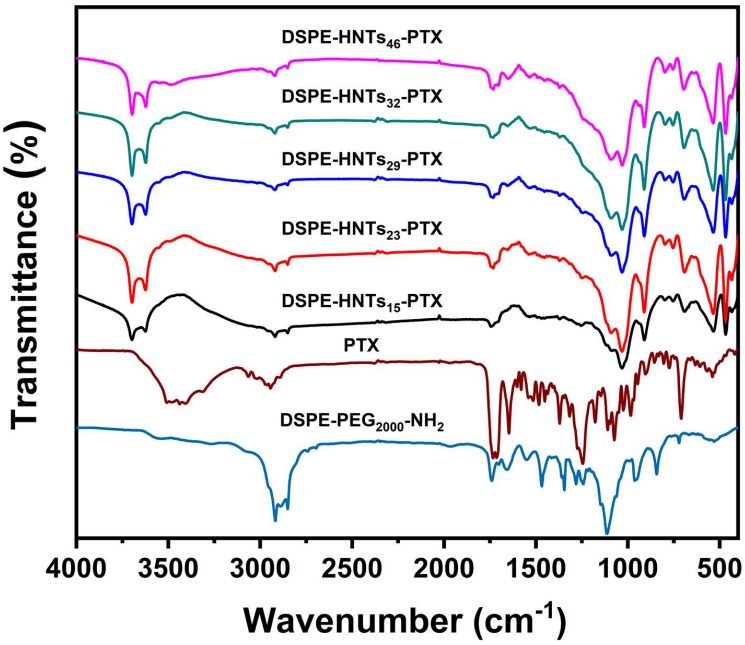

Fig. S6. FTIR spectrum of HNTs samples with different inner diameters after PTX loaded.

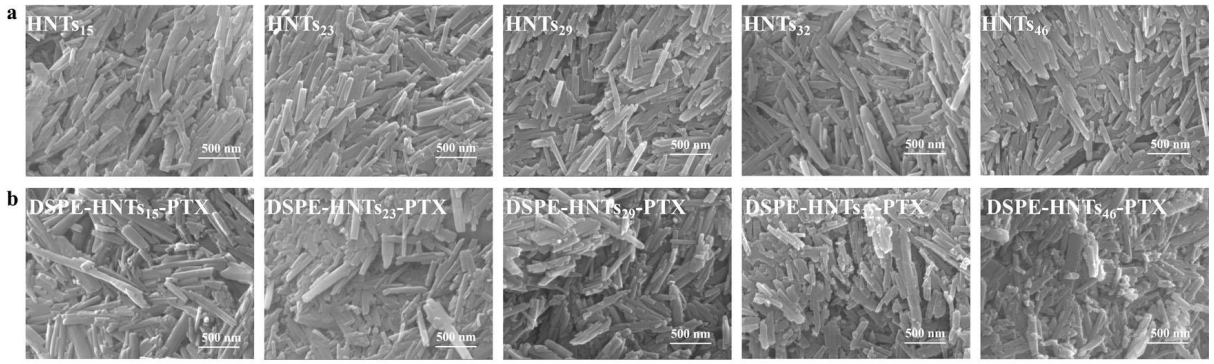

Fig. S7. SEM images of HNTs samples with different inner diameters (a) before and (b) after PTX loaded.

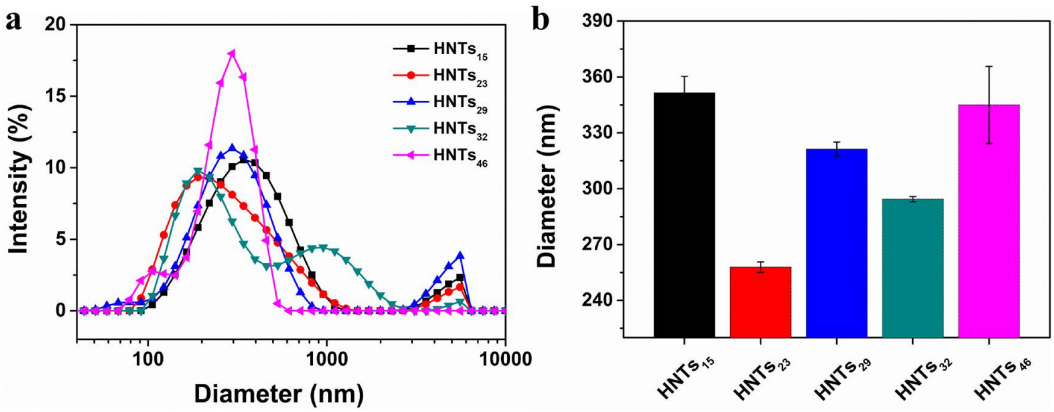

Fig. S8. (a) Particle size distribution and (b) the average particles sizes of HNTs samples with different inner diameters

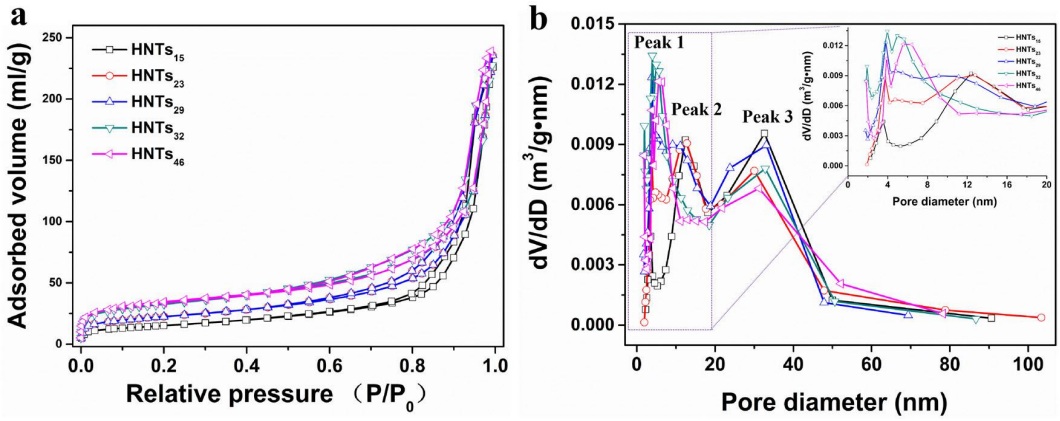

Fig. S9. (a) N_2 desorption isotherms and (b) pore size distribution curves of HNTs samples with different inner diameters.

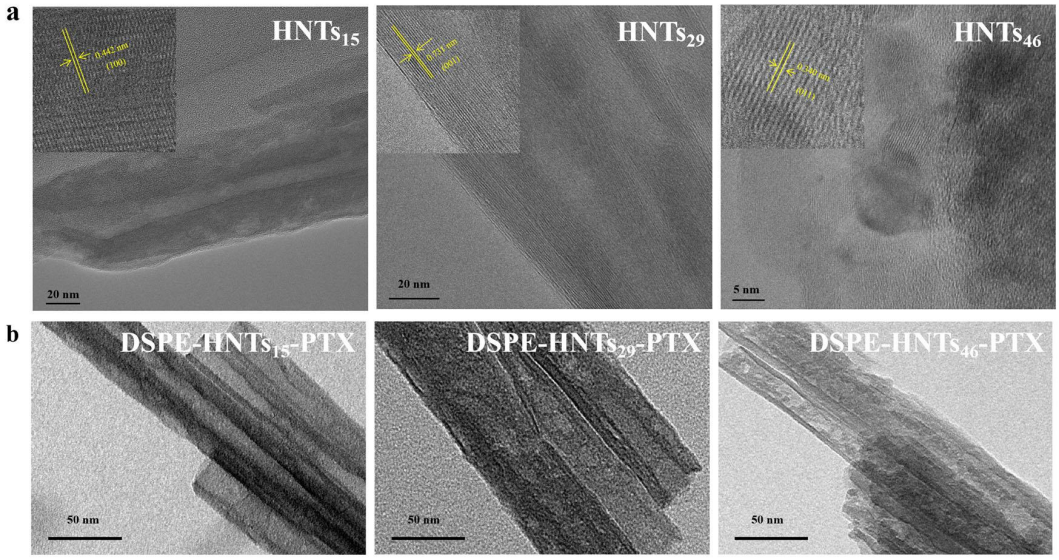

Fig. S10. TEM images of $HNTs_{15}$, $HNTs_{29}$, and $HNTs_{46}$ (a) before and (b) after PTX loaded.

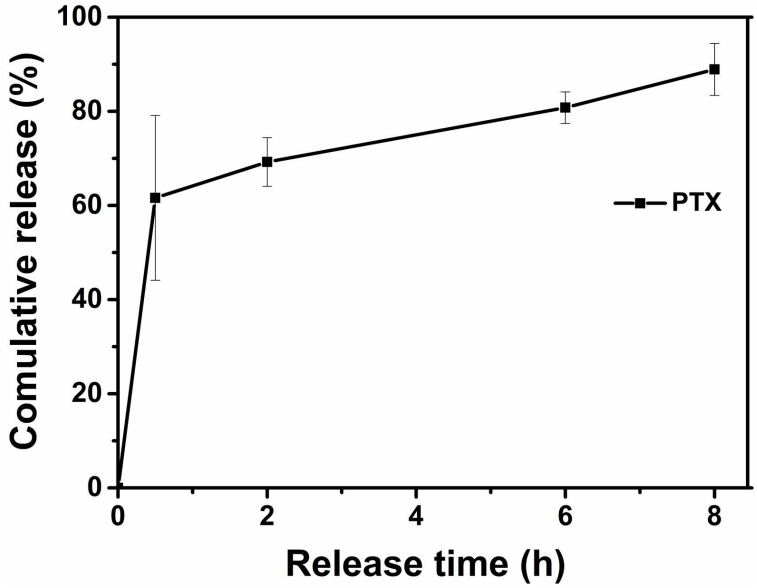

Fig. S11. *In vitro* release of PTX in pH = 7.4 PBS with 0.5% SDS.

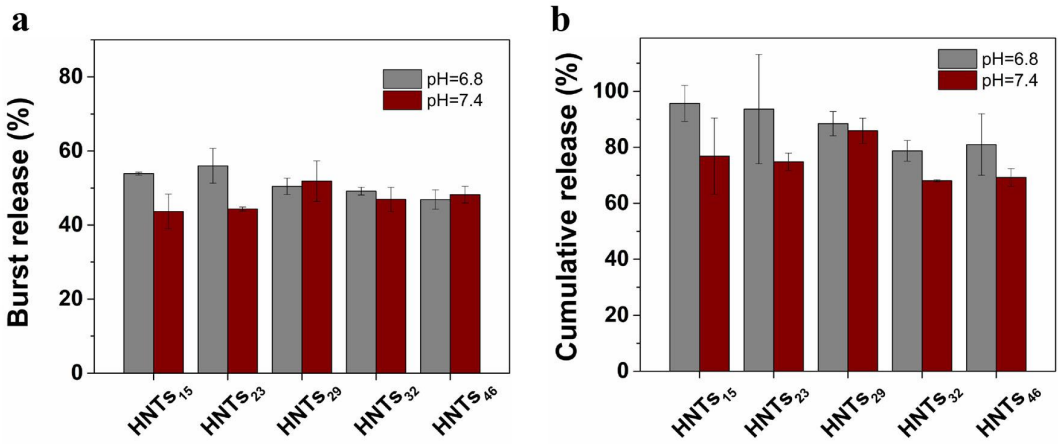

Fig. S12. (a) Burst release and (b) cumulative release of PTX from HNTs samples with different inner diameters, where burst release is quantified as percent cumulative drug release within the first 30 min and cumulative release is quantified as percent cumulative drug release at 72 h.

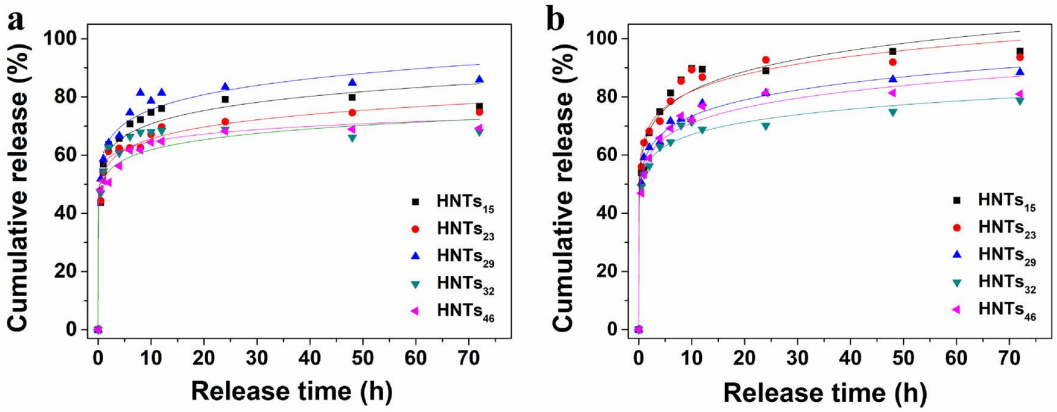

Fig. S13. Release data fits to Peppas model at (a) pH = 7.4 and (b) pH = 6.8 for HNTs samples with different inner diameters.

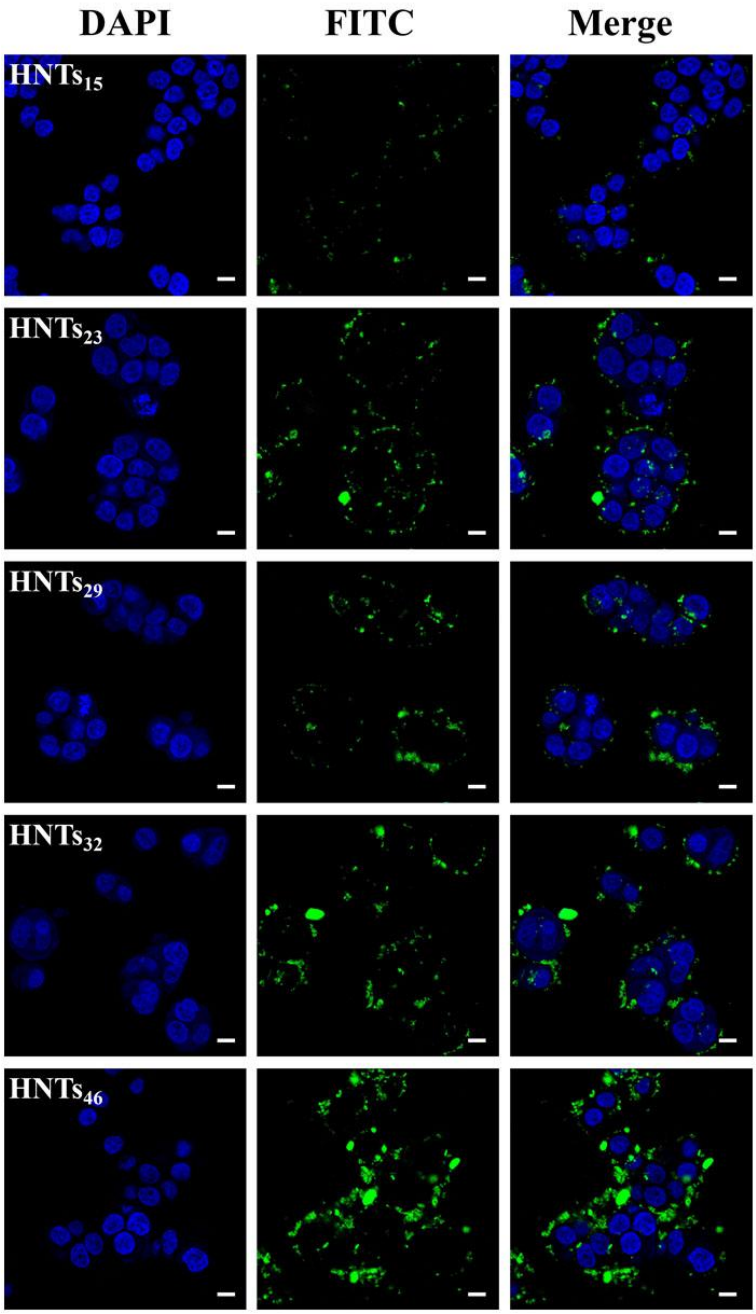

Fig. S14. Fluorescence images of HT-29 cells treated with HNT samples of different inner diameters. Scale bar: 10 μm.

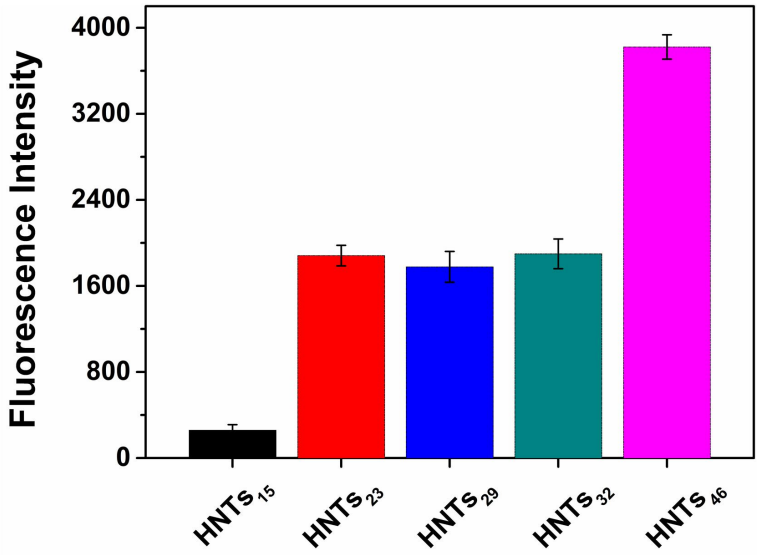

Fig. S15. FITC intensity values for the uptake of FITC-labeled HNT sample with different inner diameters.

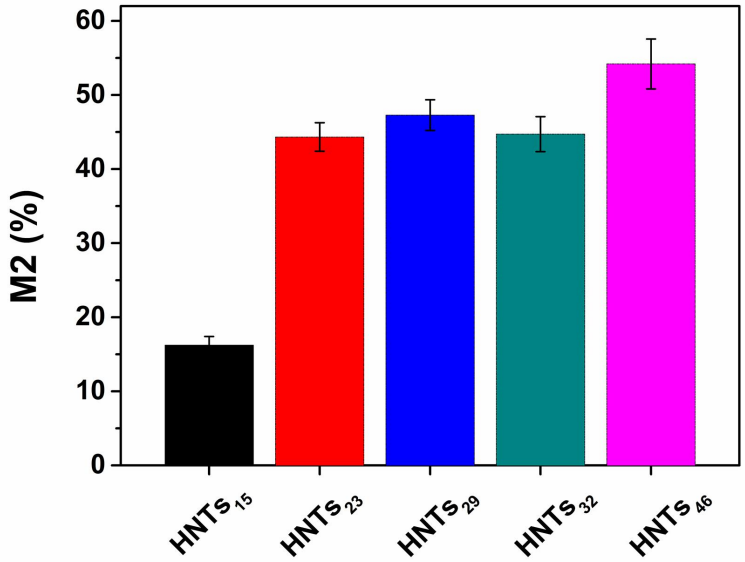

Fig. S16. Cellular uptake of HNTs samples with different inner diameters against HT-29 cells.

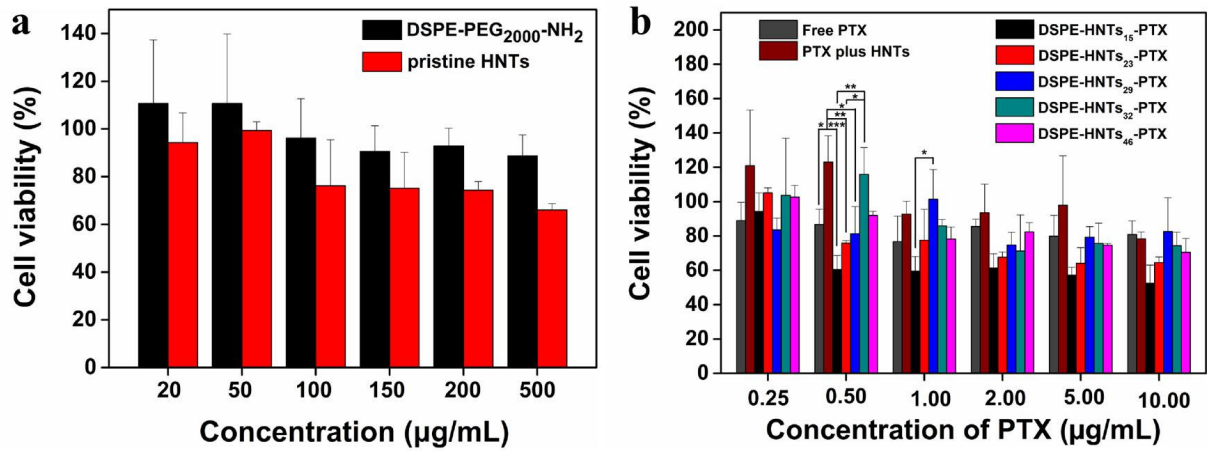

Fig. S17. Cytotoxicity of (a) DSPE-PEG_{2000}-NH_2, HNTs, and (b) free PTX, PTX plus HNTs, and HNT samples against HT-29 cells at different concentrations after 24 h, n=3. The data of cell viability were analyzed by one-way ANOVA with Tukey's post hoc test. *P < 0.05, **P < 0.01, ***P < 0.001.

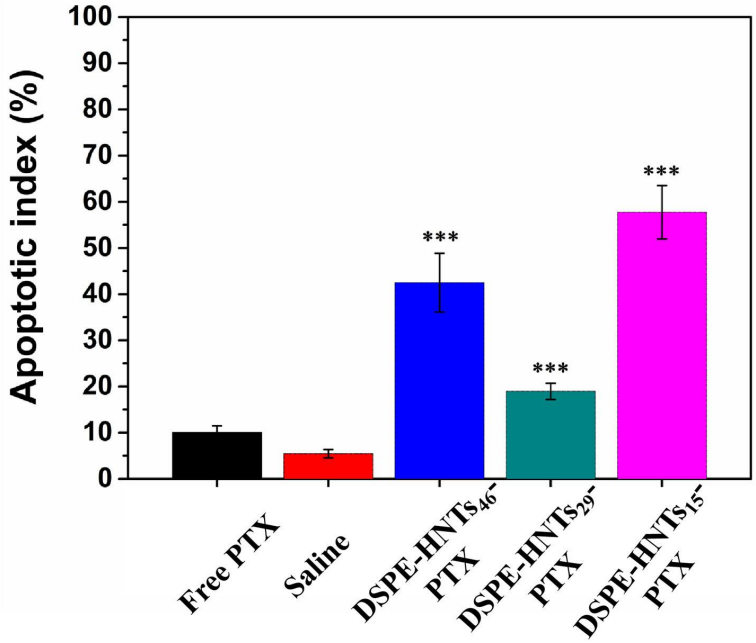

Fig. S18. Apoptosis cell number was calculated blindly in six randomly selected regions in different groups. Scale bar: 20 μm. The data of apoptosis index were analyzed by one-way ANOVA with Tukey's post hoc test. *P < 0.05, **P < 0.01, ***P < 0.001 compared to Saline group.

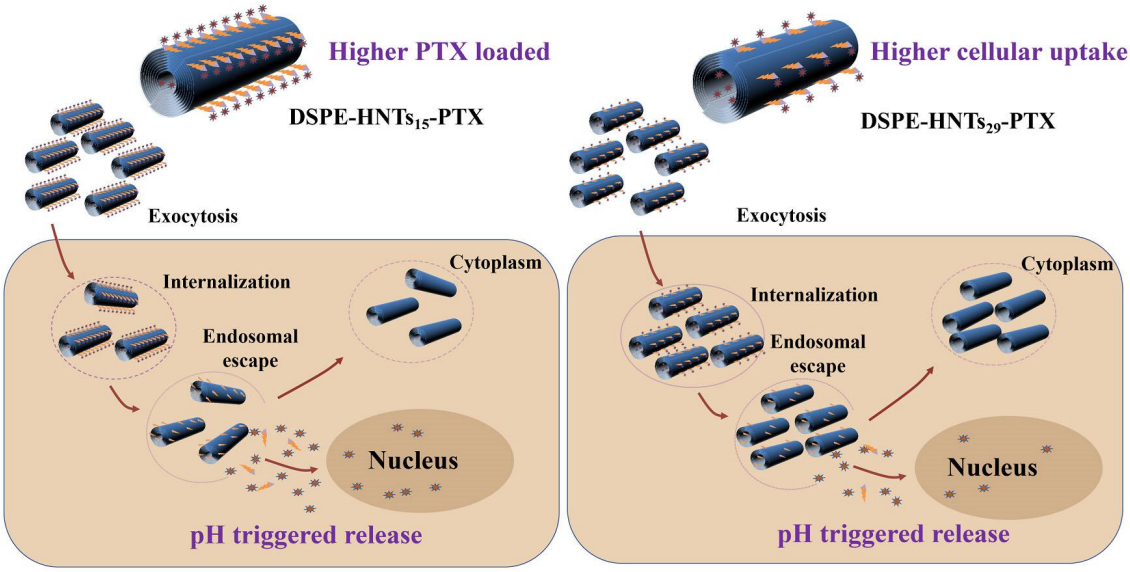

Fig. S19. Schematic illustration of DSPE-HNTs-PTX on cancer cell killing.

Table S1 The corresponding relationship between the alumina leaching rate and time.

Samples	Al leaching (%)	Time (h)
$HNTs_{15}$	0	0.0
$HNTs_{23}$	40	3.0
$HNTs_{29}$	60	4.0
$HNTs_{32}$	80	6.0
$HNTs_{46}$	90	7.0

Table S2 The drug loading capacity and encapsulation efficiency of HNTs samples with different inner diameters.

Samples	DL (%)		EE (%)	
	Average	Std	Average	Std
$HNTs_{15}$	18.44	0.37	92.19	1.84
$HNTs_{23}$	16.88	0.73	84.42	3.67
$HNTs_{29}$	14.93	0.29	74.66	1.46
$HNTs_{32}$	16.20	0.27	80.98	1.36
$HNTs_{46}$	17.55	2.11	87.75	10.56

Table S3. Comparison of PTX loading and releasing properties of DSPE-HNTs$_{15}$-PTX and other carriers.

Samples	Method	Loading Efficiency (DL%)	Encapsulation Efficiency (EE%)	Cumulative Release (%)	Application	Ref.
pGO-FA-PTX	Physically and chemically loaded	18.7	Not available	Not available	Ovarian cancer	[8]
PFA@PTX NPs	Self-assembly method	8.3	41.5	>80	colorectal cancer	[2]
PTX-TKNs	Not available	10.2	Not available	87	Cancer	[9]
PTX-HA-PLGA NPs	Nanoprecipitation method	8	80.1	69.2	Breast cancer	[10]
FMSN-PTX	Covalently linked via a disulfide linker	13	Not available	Not available	Cervical cancer	[11]
X-PLGA-SH NPs	Nanoprecipitation	39.4	99	Not available	Ovarian cancer	[12]
Standard LNCs	Mixture	Not available	99	Not available	Cancer	[13]
Neutral PTX-NPs	Not available	6.4	Not available	28	Prostate cancer	[14]
ICG/PFP@HMOP-PEG	Incorporated at the nanoparticle surface	13.8	Not available	>60	Cancer	[15]
HNT-paclitaxel	Simple mixture	7.5	Not available	80	Cervical cancer, Lung cancer	[16]
DSPE-HNTs$_{15}$-PTX	One-pot facile surfaces modification	18.4	92.2	96	Colon cancer	This work

Table S4 BET surface area, pore-volume, and average pore size of HNTs samples with different inner diameters.

Samples	S_{BET} (m^2/g)	V_T (cm^3/g)	D_A (nm)
$HNTs_{15}$	54.04	0.35	20.8
$HNTs_{23}$	79.20	0.37	17.3
$HNTs_{29}$	98.63	0.37	14.4
$HNTs_{32}$	113.48	0.36	13.1
$HNTs_{46}$	115.80	0.36	15.1

Table S5 Parameters and coefficients obtained for different release kinetic models fitted to the experimental PTX release profiles from HNTs samples with different inner diameters.

		$HNTs_{15}$	$HNTs_{23}$	$HNTs_{29}$	$HNTs_{32}$	$HNTs_{46}$
Peppas						
pH=7.4	a	57.431	53.690	60.814	56.701	51.471
	b	0.091	0.087	0.095	0.057	0.080
	R^2	0.954	0.980	0.971	0.956	0.987
pH=6.8	a	63.277	65.317	57.655	54.708	55.873
	b	0.113	0.098	0.105	0.088	0.104
	R^2	0.961	0.972	0.993	0.986	0.975
Higuchi						
pH=7.4	a	41.232	39.549	42.576	39.745	35.899
	R^2	0.929	0.922	0.907	0.906	0.883
pH=6.8	a	45.137	45.804	41.629	39.118	40.187
	R^2	0.936	0.904	0.901	0.909	0.929

Supplementary references

1 J. Liao, S. Peng, M. Long, Y. Zhang, H. Yang, Y. Zhang and J. Huang, *Colloids Surfaces A: Physicochem. Eng. Asp.*, 2020, **586**, 124242.

2 B. Jańczuk, W. Wójcik, A. Zdziennicka and J. M. Bruque, *Powder Technol.*, 1996, **86**, 229–238.

3 W. Zou, Y. Cao, J. Liu, W. Li and C. Liu, *Powder Technol.*, 2013, **246**, 669–676.

4 S. S. M. Ali, J. Y. Y. Heng, A. A. Nikolaev and K. E. Waters, *Powder Technol.*, 2013, **249**, 373–377.

5 Y. Zheng, X. You, S. Guan, J. Huang, L. Wang, J. Zhang and J. Wu, *Adv. Funct. Mater.*, 2019, **29**, 1–10.

6 L. Zhou, B. He and F. Zhang, *ACS Appl. Mater. Interfaces*, 2012, **4**, 192–199.

7 M. M. Wan, J. Y. Yang, Y. Qiu, Y. Zhou, C. X. Guan, Q. Hou, W. G. Lin and J. H. Zhu, *ACS Appl. Mater. Interfaces*, 2012, **4**, 4113–4122.

8 W. Zhuang, L. He, K. Wang, B. Ma, L. Ge, Z. Wang, J. Huang, J. Wu, Q. Zhang and H. Ying, *ACS Omega*, 2018, **3**, 2396–2405.

9 D. Chen, G. Zhang, R. Li, M. Guan, X. Wang, T. Zou, Y. Zhang, C. Wang, C. Shu, H. Hong and L. J. Wan, *J. Am. Chem. Soc*., 2018, **140**, 7373–7376.

10 J. Wu, J. Zhang, C. Deng, F. Meng and Z. Zhong, *Biomacromolecules*, 2016, **17**, 2367–2374.

11 L. Yuan, W. Chen, J. Hu, J. Z. Zhang and D. Yang, *Langmuir*, 2013, **29**, 734–743.

12 H. F. Wang, Y. Liu, T. Wang, G. Yang, B. Zeng and C. X. Zhao, *ACS Biomater. Sci. Eng.*, 2020, **6**, 5040–5050.

13 A. C. Groo, M. Bossiere, L. Trichard, P. Legras, J. P. Benoit and F. Lagarce, *Nanomedicine*, 2015, **10**, 589–601.

14 I. M. Adjei, B. Sharma, C. Peetla and V. J. Labhasetwar, *Control. Release*, 2016, **232**, 83–92.

15 J. Wu, G. R. Williams, S. Niu, F. Gao, R. Tang and L. M. Zhu, *Adv. Sci*., 2019, **6**.

16 R. Yendluri, Y. Lvov, M. M. de Villiers, V. Vinokurov, E. Naumenko, E. Tarasova and R. Fakhrullin*, J. Pharm. Sci.*, 2017, **106**, 3131–3139.